

Higher-Order Equivariant Neural Networks for Charge Density Prediction in Materials

Teddy Koker^{1*}, Keegan Quigley¹, Eric Taw^{1,2}, Kevin Tibbetts¹,
and Lin Li^{1*}

¹MIT Lincoln Laboratory, Lexington, MA 02421

²Material Science Division, Lawrence Berkeley National Laboratory, Berkeley, CA 94720

*Correspondence to {thomas.koker, lin.li}@ll.mit.edu

Abstract

The calculation of electron density distribution using density functional theory (DFT) in materials and molecules is central to the study of their quantum and macro-scale properties, yet accurate and efficient calculation remains a long-standing challenge in the field of material science. This work introduces ChargeE3Net, an $E(3)$ -equivariant graph neural network for predicting electron density in atomic systems. ChargeE3Net achieves equivariance through the use of higher-order tensor representations, and directly predicts the charge density at any arbitrary point in the system. We show that our method achieves greater performance than prior work on large and diverse sets of molecules and materials, and scales to larger systems than what is feasible to compute with DFT. Using predicted electron densities as an initialization, we show that fewer self-consistent iterations are required to converge DFT over the default initialization. In addition, we show that non-self-consistent calculations using the predicted electron densities can predict electronic and thermodynamic properties of materials at near-DFT accuracy.

1 Introduction

Electronic charge density is one of the most fundamental quantities in quantum chemistry and physics, and it is key to accurately modeling molecules and materials at the atomic scale. The Hohenberg-Kohn theorem [1] states that the ground-state charge density contains the information necessary to obtain all ground-state properties of interest. The Kohn-Sham (KS) formulation of density functional theory (DFT) [2] is the most widely used ab initio method for performing electronic structure calculation of molecules or materials. However, KS-DFT is computationally expensive with $O(N^3)$ complexity, making it

infeasible for large-scale quantum calculations on classical computers beyond a few hundred atoms.

More recently, machine learning models have been developed to overcome the computational challenge of ab initio calculations, but they rely on custom-fitted basis functions. Early approaches using machine learning for the prediction of electron density were based on the use of symmetry-adapted Gaussian process regression to predict coefficients for atom-centered basis functions [3, 4]. Coefficients are predicted from a kernel function that expresses the structural similarity and geometric relationship among a target atomic environment and a training set of atomic environments. More recent work has leveraged invariant and equivariant neural networks to predict these coefficients from atomic features. Qiao et al. [5] uses features computed by density-functional tight-binding [6] as inputs for a higher-order equivariant neural network to predict basis set coefficients of small molecules found by self-consistent DFT calculations. Rackers et al. [7] use a higher-order equivariant neural network to predict basis set coefficients directly from atomic graphs. While these approaches are able to achieve high accuracy in specific settings, they are limited by the expressivity of the density fitting basis sets. These atom-centered basis sets are typically defined per-species and are numerically more difficult to converge for solid-state systems compared to plane-wave basis sets, limiting their applicability to molecular systems in vacuum [8].

Alternatively, several methods were proposed to learn electron density directly from a discretized grid of density points. Charge density predictions on grids are agnostic to the basis set used for the ground-truth quantum chemistry calculation and are a natural input format for popular plane-wave DFT codes. By inserting each grid or “probe” point into the atomic graph, charge density prediction can be modeled as a node regression task [9–12]. However, most of these models only focus on small and specialized atomic systems. Gong et al. [9] use an invariant graph convolutional network [13] to train a charge density model on a small dataset of crystalline polymers, demonstrating transferability to unseen structures. Jørgensen and Bhowmik [10] similarly use an invariant graph convolutional network, SchNet [14], demonstrating fast and high accuracy charge density prediction in small molecules, lithium ion battery (LIB) cathode materials and LIB electrolytes. They later demonstrate an improvement in accuracy through the use of an equivariant graph convolutional network, PaiNN [11], through \mathbb{R}^3 vector representations and rotationally equivariant operations [15]. While these models have been shown to achieve high accuracy when trained and evaluated on small, specialized molecular or material datasets, their expressive power on larger, diverse datasets such as the Materials Project [16] is not yet understood. Furthermore, these models use scalar and/or vector representations to construct rotationally equivariant networks, which could be further improved by incorporating higher-order equivariant features, as has been shown in other tasks, such as the prediction of atomic forces [17].

In this work, we develop a neural network model, ChargE3Net, that uniquely

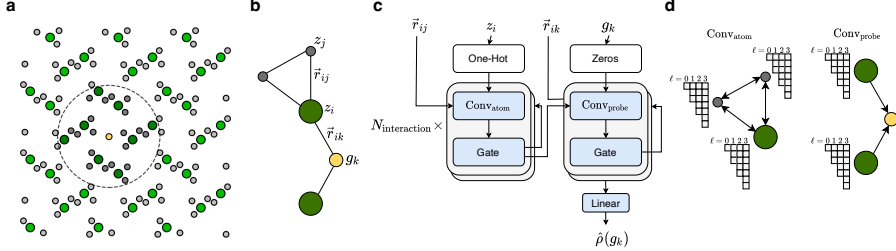


Figure 1: **Overall architecture of the ChargeE3Net model.** a: Illustration of single charge density probe point, shown in yellow, and its local environment within a periodic atomic system. b: Sub-graph of local environment graph with atom nodes z_i , z_j and probe node g_k . c: Neural network architecture. Predicted charge density $\hat{\rho}(\vec{g})$ at probe point \vec{g}_k is computed from the atomic species z_i , interatomic displacement vectors r_{ij} , and probe-atom displacement vectors r_{ik} through a series of convolution and gate operations. d: $\text{Conv}_{\text{atom}}$ sends higher-order representations bidirectionally to atom nodes. $\text{Conv}_{\text{probe}}$ sends higher-order representations from atoms to probes.

combines graph neural networks, $\text{SO}(3)$ equivariant features, and higher-order tensor operations, to accurately predict the electron density of a given atomistic system. Our method enables the use of higher-order equivariant features to better capture the angular resolution and directional information. In a head-to-head comparison, we show that our method achieves greater accuracy than prior work in the prediction of charge density on a diverse sets of density data for both materials and organic molecules. More remarkably, our method outperforms prior models relying on features obtained through quantum mechanical simulation, demonstrating the ability of our approach to learn complex atomic and subatomic interactions from only atomic configurations. Our model trained on over 120K charge density calculations performed by Material Project further demonstrates the expressivity of ChargeE3Net, making it applicable to crystalline materials containing any element and of any materials class. To investigate the effect of higher-order representations, we quantify the angular dependence of the charge density at each grid point and show that higher-order representations yield more accurate charge density predictions for materials with high angular variation. We demonstrate the linear time complexity of our model with respect to system size, showing the capability of predicting density on systems with $> 10^4$ atoms, surpassing what is feasible with ab initio calculations. Lastly, we show that the predicted densities accelerate DFT calculations by reducing the self-consistent steps required to reach a converged solution, and demonstrate the application of using the predicted charge densities to compute a wide range of electronic and thermodynamic properties non-self-consistently, achieving near-DFT accuracies for a majority of materials in a held-out test set.

2 Results

2.1 Development of higher-order equivariant neural networks for charge density prediction

Given an atomic system (atomic positions and species), we seek to predict the electron charge density $\rho(\vec{r}) : \mathbb{R}^3 \rightarrow \mathbb{R}$ at any point within the atomic system. The charge density, along with other properties such as forces, is equivariant under rotation and translation of the atomic system. That is, a rotation or translation of the atomic system in Euclidean space will result in an equivalent rotation or translation to the charge density or forces. Formally this is known as equivariance with respect to $E(3)$, which includes rotations, translations, and reflections in 3D space. This can be achieved in principle by using only invariant scalar features [14], such as inter-atomic distances; however, this prevents the model from using angular information, limiting the accuracy that can be attained [18]. More recent work [15] has introduced equivariance methods using vector \mathbb{R}^3 features, such as relative atomic positions, to incorporate angular information, and has been shown to improve the performance of charge density prediction [11].

ChargE3Net achieves equivariance through means outlined by tensor field networks [19]. Translation equivariance is achieved by using relative atomic positions; rotation equivariance is achieved by restricting features to be irreducible representations, *irreps*, of $SO(3)$, which are operated upon by equivariant functions. These features take the form $V_{cm}^{(\ell,p)}$, a dictionary of tensors with keys representing rotation order $\ell \in \{0, 1, 2, \dots\}$ and parity $p \in \{-1, 1\}$. Each tensor has a channel index $c \in [0, N_{\text{channels}})$ and an index $m \in [-\ell, \ell]$. In this way, the representation at a given ℓ and p will have a size of $\mathbb{R}^{N_{\text{channels}} \times (2\ell+1)}$. These representations are combined with the equivariant tensor product operation \otimes , using Clebsch–Gordan coefficients C as described in [19] and implemented in `e3nn` [20]:

$$\left(U^{(\ell_1, p_1)} \otimes V^{(\ell_2, p_2)} \right)_{cm_o}^{(\ell_o, p_o)} = \sum_{m_1=-\ell_1}^{\ell_1} \sum_{m_2=-\ell_2}^{\ell_2} C_{(\ell_1, m_1)(\ell_2, m_2)}^{(\ell_o, m_o)} U_{cm_1}^{(\ell_1, p_1)} V_{cm_2}^{(\ell_2, p_2)} \quad (1)$$

where ℓ_o and p_o are given by $|\ell_1 - \ell_2| \leq \ell_o \leq |\ell_1 + \ell_2|$ and $p_o = p_1 p_2$. We maintain only those representations with $\ell_o \leq L$ where L is a maximum allowed rotation order. For ease of notation, we will omit the keys ℓ, p and indices c, m for these tensor representations for the rest of the paper.

Fig. 1 shows the model architecture of ChargE3Net. To predict charge density of a given atomic system, a set of M probe points $\{\vec{g}_1, \dots, \vec{g}_M\} \in \mathbb{R}^3$ are introduced to locations where charge densities are to be predicted. We represent predicted charge density $\hat{\rho}(\vec{g})$ as an equivariant graph neural network with inputs of atomic numbers $\{z_1, \dots, z_N\} \in \mathbb{N}$ with respective locations of the atoms $\{\vec{r}_1, \dots, \vec{r}_N\} \in$

\mathbb{R}^3 where N denotes the total number of atoms, as well as probe locations $\{\vec{g}_1, \dots, \vec{g}_M\} \in \mathbb{R}^3$ and an optional periodic boundary cell $B \in \mathbb{R}^{3 \times 3}$ for periodic systems.

As illustrated in Fig. 1(a) and (b), a graph is first constructed with atoms and probe points as vertices, with edges formed via proximity with a cutoff of 4 Å. Edges connecting atoms are unidirectional and edges connecting atoms and probe points are directed pointing from atoms to probe points. Vertex features for atoms $\{A_i\}_{i=0}^N$ are initialized as a one-hot encoding of the atomic number, represented as a $\ell = 0, p = 1$ tensor with N_{channels} equal to the number of atomic species. Features for probe points $\{P_k\}_{k=0}^M$ are initialized as a single scalar zero (i.e., $\ell = 0, p = 1$ and $N_{\text{channels}} = 1$).

ChargE3Net uses a graph neural network (GNN) to update these tensor features, as shown in Fig. 1(c). Within each layer of GNN, the network performs message passing between neighboring atoms and probes, where probe points can only receive messages from neighboring atoms; See Fig. 1(d). The core of the message passing in ChargE3Net is a convolution function that updates the vertex tensor feature with neighboring vertices by the convolution operation defined in Eqn. (4) in Methods. The proposed convolution operation replaces the linear message passing with equivariant operation through tensor product as shown in Eqn. (1) and thus is rotation and translation equivariant; see Methods for more detail. This is then followed by an equivariant Gate activation operation.

ChargE3Net conducts a series of convolution and gate operations. The learned tensor feature associated to each probe point is passed to a post-processing layer where a simple regression decision-head is used to predict the charge density at the corresponding probe location $\hat{\rho}(\vec{g}_k)$.

2.2 Performance evaluation

We train and validate ChargE3Net on a diverse set of DFT-computed charge density data, including organic molecules (QM9) [21–23], nickel manganese cobalt battery cathode materials (NMC) [24], and inorganic materials collected from Materials Project (MP) [16, 25]. The first two datasets have been used in the past for benchmarking charge density models for small molecules and a subset of crystal systems with boundary conditions [5, 11]. To broaden the applicability of the model beyond small, specialized atomic systems, we investigate a more diverse dataset from the MP database, which includes charge densities for over 120K bulk materials. See the Methods section for details of the datasets and the training procedure.

We assess the performance our models using mean absolute error normalized by the total number of electrons within a volume of the atomic system [3–5, 11], ϵ_{mae} , which is computed via numerical integration on the charge density grid points G :

Table 1: Error for each dataset, reported in average ϵ_{mae} (%), \pm one standard error. Bold values represent the best ϵ_{mae} (%) scores.

Dataset	invDeepDFT	equiDeepDFT	OrbNet-Equi	ChargE3Net
NMC	0.089 ± 0.001	0.061 ± 0.001	-	0.060 ± 0.001
QM9	0.357 ± 0.001	0.284 ± 0.001	0.206 ± 0.001	0.196 ± 0.001
MP	0.859 ± 0.011	0.799 ± 0.010	-	0.523 ± 0.010

$$\epsilon_{\text{mae}} = \frac{\sum_{\vec{g}_k \in G} |\rho(\vec{g}_k) - \hat{\rho}(\vec{g}_k)|}{\sum_{\vec{g}_k \in G} |\rho(\vec{g}_k)|} \quad (2)$$

Unless otherwise noted, the probe points G hereby reference the full set of discretized unitcell grid points for which we have DFT-computed charge density values.

We compare the performance of ChargE3Net to models introduced in OrbNet-Equi [5] and DeepDFT [11]. For QM9 and NMC datasets we use identical training, validation, and test splits as Jørgensen and Bhownik [11], and report ϵ_{mae} computed using the authors publicly released models. We verify these to match the numbers reported in the authors' original work. For the MP dataset, we train the DeepDFT models using the same experimental settings from the original work. As shown in Table 1, ChargE3Net model significantly outperforms the prior equivariant DeepDFT models [11] on the Materials Project (MP) and QM9 datasets, while achieving similar performance on the NMC dataset. More remarkably, our model achieves a lower ϵ_{mae} on the QM9 dataset than OrbNet-Equi [5] model, which leverages additional features based on quantum mechanical calculations while ChargE3Net only uses atomic species and position information. This shows how the model is capable of learning highly informative representations of quantum interactions in a purely data-driven manner.

ChargE3Net's performance on the MP data demonstrates that it is capable of successfully modelling charge density across the periodic table and a wide variety of material classes that are not present in the other datasets. This suggests ChargE3Net can reproduce a broad range of chemical interactions at the electronic level without incurring the cost of an ab initio calculation. Our results shown in Table 1 also reveal the importance of respecting rotation equivariance in constructing such a general model.

2.3 Effects of higher-order representations

To demonstrate the impact of introducing higher-order equivariant tensor representations in our model, we examine the effect of training models while varying the maximum rotation order L , with $\ell \in \{0, \dots, L\}$ up to $L = 4$. While higher-order representations are achievable, they can be prohibitive to use in

the network due to the $O(L^6)$ computational complexity of tensor products [26]. We determine the number of channels for each rotation order by $N_{\text{channels}} = \lfloor \frac{500/(L+1)}{\ell*2+1} \rfloor$. For example, the $L = 0$ model has representations consisting of 500 even scalars, and 500 odd scalars, while the $L = 1$ model has representations consisting of 250 even scalars, 250 odd scalars, 83 even vectors, and 83 odd vectors. In this way, each model is constructed such that the total representation size and the proportion of the total representation used by each rotation order are approximately equal. We train each model on 1,000, and 10,000 material subsets and the full MP dataset, using the same validation and test sets. As shown in Fig. A.1, we observe a consistent increase in performance on each training subset as the maximum rotation order increases, and a similar scaling behavior with respect to the training set size. This trend suggests that higher-order representations are necessary for accurate charge density modeling, and can match the performance of lower order models with less data.

To gain intuition behind why and when higher-order representations yield higher performance, we investigate two factors contributing to the variance of charge density within a material: (1) *radial* dependence, or a dependence on the distance from neighboring atoms, and (2) *angular* dependence, or dependence on angular orientation with respect to those atoms and the larger atomic system. While most materials exhibit strong radial dependence, some also exhibit strong angular dependence. For example, materials with covalent bonds share electrons between nucleii, leading to higher charge density along bonding axes and more angular dependence. In Fig. 2, we illustrate this concept with two materials. $\text{Cs}(\text{H}_2\text{PO}_4)$ exhibits high angular dependence, where charge density is dependent on angle as well as radial distance from the nearest atom. The complex nature of the charge density shown here arises from covalent bonding among the H, P, and O atoms. Conversely, Rb_2Sn_6 does not exhibit this, as its density appears to be almost entirely a function of the atomic distance, suggesting that a lower-order equivariant or invariant architecture could model its electron density well. This may be indicative of ionic interactions rather than the covalent interactions found in $\text{Cs}(\text{H}_2\text{PO}_4)$. We find this intuition to be consistent with model performance, as Fig. 2 shows similar performance for $L = 0$ and $L = 4$ models for Rb_2Sn_6 , while the $L = 4$ model exceeds the performance of the $L = 0$ model for $\text{Cs}(\text{H}_2\text{PO}_4)$.

At the atomic level, we find more evidence of the benefits of higher-order equivariant representations in modeling charge density. We examine the per-element errors by computing ϵ_{mae} on grid points $G_{\text{local},i} \subset G$, a set of points that are within 2Å of an atom of species i . Figure 3 shows this per-element error, averaged across the test set. While the $L = 0$ model struggles with reactive non-metals and metalloids, which often form covalent bonds, $L = 4$ shows strong improvement among these elements. Nearly all elements show improvement, but the median change in ϵ_{mae} values for those materials containing a non-metal or metalloid is -44.6% ($n = 1628$) compared to -23.0% for materials with only metals ($n = 346$) (Fig. A.2).

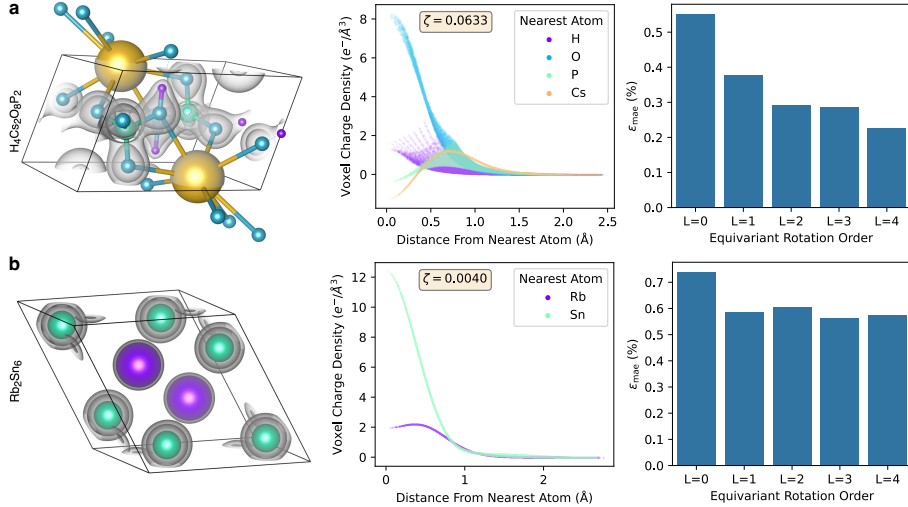


Figure 2: **Effect of angular variance.** Comparison of material with high angular variance $\text{Cs}(\text{H}_2\text{PO}_4)$ (a) and low angular variance Rb_2Sn_6 (b), as determined by 95th- and 5th-percentile ζ values in test set. Left to right: visualization of charge density isosurfaces (gray); plot of DFT-computed charge density with respect to radial distance from nearest atom; ϵ_{mae} for ChargE3Net model predictions on these materials.

To further quantify angular dependence within the system, we develop a metric ζ to determine to what extent a particular system exhibits more angular variation in its charge density with respect to atom locations. This is achieved by measuring the dot product of the unit vector from a probe point to its nearest neighboring atom and the gradient of the density at that probe point:

$$\zeta(G) = 1 - \frac{\sum_{\vec{g}_k \in G} |\nabla \rho(\vec{g}_k) \cdot \hat{r}_{ki}|}{\sum_{\vec{g}_k \in G} \|\nabla \rho(\vec{g}_k)\|} \quad (3)$$

where G is a set of probe points and \hat{r}_{ki} is a unit vector from probe point at location \vec{g}_k to the closest atom at location \vec{r}_i . Intuitively, a material with charge density gradients pointing directly towards or away from the nearest atom will have dot products larger in magnitude and $\zeta \rightarrow 0$, whereas a material with density that has high angular variance with respect to the nearest atom will have dot products smaller in magnitude, and $\zeta \rightarrow 1$. Figure A.3 shows the test set average ζ over $G_{\text{local},i}$ for every element. Figure A.4 demonstrates that the differences in performance between the lower and higher rotation order networks correlates strongly with ζ . With covalent bonding and associated high angular variance frequently present in the Materials Project data, this further justifies the need for introducing higher rotation order representations into charge density prediction networks.

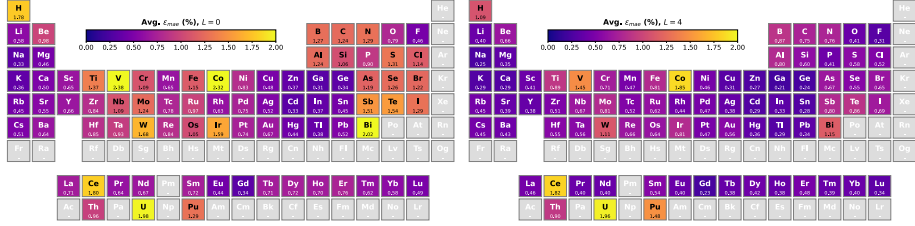


Figure 3: **Effect of rotation order on element-wise error.** Average ϵ_{mae} per element at $L = 0$ (left) and $L = 4$ (right), showing performance improvements across the periodic table. Values are computed over the set of grid points G_{local} , and averaged across all materials containing those elements in the test set. Only elements in at least 10 test set materials are shown.

2.4 Runtime and scalability

To demonstrate the scalability of our model, we analyze the runtime duration of our model on systems with increasing number of atoms, and compare to the duration of DFT calculations. We run each method on a single material, BaVS₃ (mp-3451 in MP), creating supercells from $1 \times 1 \times 1$ to $10 \times 10 \times 10$ and recording the runtime to generate charge density of the system. Figure 4(a) shows an approximate linear, $O(N)$, scaling of our model with respect to number of atoms, while DFT exhibits approximately $O(N^{2.3})$ before exceeding our computational budget. This is to be expected, as the graph size increases linearly with cell volume if the resolution remains the same, while DFT has shown to scale at a cubic rate with respect to system size [11]. Furthermore, our method can be fully parallelized up to each point in the density grid with no communication overhead.

2.5 Using predicted charge densities to accelerate DFT

DFT calculations require an initial charge density and wavefunction prior to iteratively solving the Kohn-Sham equations until self-consistency [27]. Charge density initializations that closely match the ground-state charge density often save compute time by reducing the number of self-consistent field (SCF) steps needed to find a self-consistent solution. Many schemes for initializing the charge density exist in the literature, but perhaps the most common one is the superposition of atomic densities (SAD), where the initial charge density is computed by summing over the atomic charge density of each atom in the system [28].

We show that charge densities predicted by ChargE3Net reduce the number of SCF steps, thereby accelerating DFT calculations, on unseen non-magnetic materials (see Fig. 4b) compared to a SAD initialization. The median number of SCF steps needed to converge a single-point calculation self-consistently for a non-magnetic material starting from the SAD initialization is 15, while the same

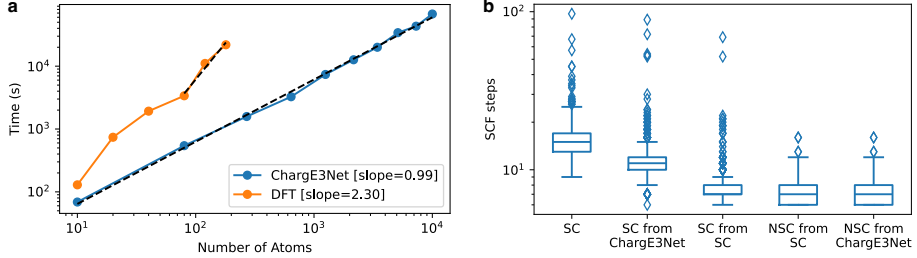


Figure 4: Runtime and acceleration of DFT. a: Runtime comparison of DFT and our ChargE3Net model with respect to number of atoms in the evaluated system. DFT is using a 48-core Intel Xeon CPU, while ChargE3Net uses a single NVIDIA V100 GPU. b: Number of SCF steps required to reach an energy change threshold of 10^{-5} for non-magnetic materials in the test set. Box plot edges show 25th and 75th percentiles, while the white line in the box plot shows the median. SC = self-consistent calculations starting from SAD. SC from ChargE3Net = self-consistent calculations starting from a charge density estimate with ChargE3Net. SC from SC = self-consistent calculation using a charge density initialized from the SC calculation of the same material. NSC from x = non-self-consistent calculation using the x starting point.

starting from a ChargE3Net initialization is 11, representing a 26.7% decrease in SCF steps. As a benchmark, we also include the distribution of the number of SCF steps needed to converge a calculation starting from a converged (ie ground-truth) charge density (“SC from SC”), showing that our model still has room for improvement. About 96% of calculations done with a predicted charge density ran with fewer SCF steps than initializing with SAD, and the compute time improvement is robust to a wide range of ϵ_{mae} (see Fig. A.7).

In Fig. 5 we compute the energy, forces, band energies, and bandgaps of the test set non-self-consistently to evaluate how well ChargE3Net’s predicted charge densities reproduce physical properties. 39% of materials in the test set have per-atom energy errors less than 1 meV/atom. 67% of materials have forces less than 0.03 eV/Å, a common threshold for structural relaxations; 15% of the test set have force errors of 0.0. All of the structures with perfect agreement have self-consistent forces of 0.0 eV/Å for each atom and Cartesian component, possibly because of cancellation of charge density errors due to symmetry. 43% and 75% of materials recover band energies at each k-point and the direct band gap within chemical accuracy (43 meV), respectively. 45% of the band gaps obtained non-self-consistently exactly matched those of self-consistent calculations. Similar to the force data described above, calculations with perfect agreement all have a self-consistent band gap of 0 eV, indicating the model is able to readily identify metallic materials. We note that our use of chemical accuracy for band gaps is a more stringent criterion than experimental measurement errors for well-studied semiconductors [30].

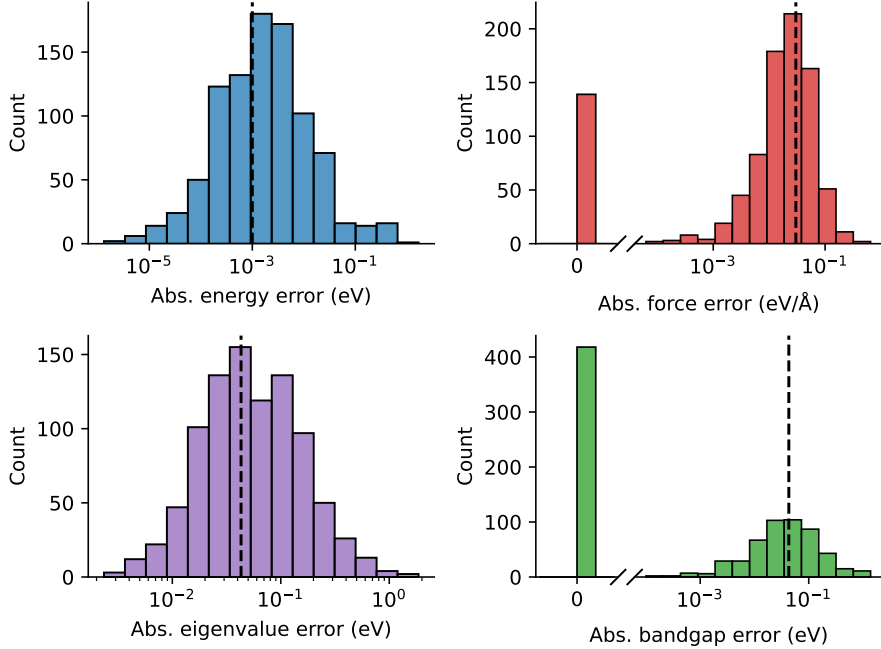


Figure 5: **Non-self-consistent physical property calculation.** Absolute errors of the total energy normalized by the number of atoms (top right), atomic forces (top left), band energies (bottom right), and band gaps (bottom left). Dashed lines indicate chemical accuracy (43 meV) except for per-atom energies, which is 1 meV/atom, and forces, which is 0.03 eV/Å.

In addition to the model’s robustness to materials outside its training set, we show that ChargE3Net can predict the charge densities of materials after small atomic perturbations with minor increase to the charge density error (see Fig. A.6). This allows us to accurately obtain phonon properties, which may rely on finite differences as the main method to obtain approximations to the local potential energy surface, from non-self-consistent calculations. We compute the constant-volume heat capacity (C_v) under the harmonic approximation for two zeolites, which are not included in the Materials Project dataset, and show that $C_v(T)$ obtained closely match those obtained by self-consistent calculations (see Section A.1). As another example of transferability, we compute the electronic bandstructure of the Si(111)-2x1 surface non-self-consistently from the ChargE3Net prediction and show that it almost exactly matches that of a self-consistent calculation (see Section A.2).

3 Discussion

This work introduces ChargE3Net, an architecture for predicting charge density through equivariance with higher-order representations. We demonstrate that introducing higher-order tensor representations over scalars and vectors used in prior work achieves greater predictive accuracy, and show how this is achieved through the improved modelling of systems with high angular variance. ChargE3Net enables accurate charge density calculations on atomic systems larger than what is computationally feasible with DFT, but can also be used in combination with self-consistent DFT to reduce the number of SCF steps needed for convergence. Our findings hold across the large and diverse Materials Project dataset, paving the way towards a universal charge density model for materials.

The work of Hohenberg and Kohn proves that all material properties could, in principle, be derived from the electron density [1]. Because this quantity is so fundamental to predicting material properties, we view models that compute electron densities as a potential intermediate towards other material properties that may improve the generalizability of machine learning models in material science. This leads us to believe that large models trained on a dataset that spans the known material space could be a promising direction towards a foundation model for DFT calculations that can be fine-tuned for additional properties. As evidence, our non-self-consistent calculations, which can be seen as a ground-truth calculation of the electronic structure (and derived properties) using the crystal structure and charge density as inputs, demonstrate that one could indeed obtain electronic and thermal properties of materials using highly accurate charge-density estimates (see Sections A.1 and A.2). On a broader dataset, we show that non-self-consistent calculations are able to capture the total energy, atomic forces, electronic bandstructure, and the band gap within chemical accuracy for a majority of structures in the test set, though there is room for improvement. We show in Fig. A.8 - A.13 that errors in the charge density establish a lower bound to the property error, and that small charge density errors can give rise to substantial property error. We hypothesize that small errors localized around atomic nuclei could be the reason for higher than expected property errors, though further study is needed to confirm this.

While higher order $SO(3)$ equivariant tensor operations yield significantly improvement in charge density predictions (Fig. 2 and 3), the $SO(3)$ convolution used in this work are limited by the $O(L^6)$ time complexity of tensor products. Recent work [26] has demonstrated that $SO(3)$ convolutions can be reduced to $SO(2)$, with a time complexity of $O(L^3)$. In the future, our approach can be combined with the methodology presented in [26] to improve computational efficiency, and enable the practical usage of higher rotation orders ($L \gg 4$) in atomistic modeling.

We also anticipate extending our model to include the spin density, which will allow for acceleration of DFT calculations of magnetic materials. Training

ChargE3Net with energies and forces would allow for rapid identification of the lowest energy magnetic configuration, a normally laborious and time-intensive process [31, 32], and the ability to obtain magnetic properties, such as the Curie temperature.

4 Methods

4.1 Architecture

A^n is initialized as a one-hot encoded z , represented as a $\ell = 0, p = 1$ tensor with N_{channels} equal to the number of atomic species. P^n is initialized as single scalar zero, with $\ell = 0, p = 1$, and $N_{\text{channels}} = 1$. Each representation is updated through a series of alternating convolution $\text{Conv}(\cdot)$ and non-linearity $\text{Gate}(\cdot)$ layers, a total of $N_{\text{interactions}} = 3$ times. With each convolution layer, all possible outputs of the tensor product at different ℓ and p values with $\ell_o \leq L$ are concatenated, increasing the representation size past the scalar initializations of A^n and P^n . Atom representations are updated with $A_i^{n+1} = \text{Gate}(\text{Conv}_{\text{atom}}^n(\vec{r}_i, A_i^n))$. $\text{Conv}_{\text{atom}}$ is defined as:

$$\text{Conv}_{\text{atom}}^n(\vec{r}_i, A_i^n) = W_1^n \left(\sum_{j \in N(i)} W_2^n A_j^n \otimes R(r_{ij}) Y(\hat{r}_{ij}) \right) + W_3^n A_i^n \quad (4)$$

where W_1, W_2, W_3 are learned weights applied as a linear mix or self-interaction [19]. The set $N(i)$ includes all atoms within the cutoff distance, including those outside potential periodic boundaries. r_{ij} is the distance from \vec{r}_i and \vec{r}_j , with unit vector \hat{r}_{ij} . $Y(\hat{r}_{ij})$ are spherical harmonics, and $R(r_{ij}) \in \mathbb{R}^{N_{\text{basis}}}$ is a learned radial basis function defined as:

$$R(r_{ij}) = \text{MLP}([\phi_1(r_{ij}), \dots, \phi_{N_{\text{basis}}}(r_{ij})]) \quad (5)$$

where $\text{MLP}(\cdot)$ is a two layer multilayer perceptron with SiLU non-linearity [33], $\phi(\cdot)$ is a Gaussian basis function $\phi(r_{ij})_k \propto \exp(-(r_{ij} - \mu_k)^2)$ with μ_k uniformly sampled between zero and the cutoff, then normalized to have a zero mean and unit variance.

The convolution updates the representation of each atom to be the sum of tensor products between neighboring atom representations and the corresponding spherical harmonics describing their relative angles, weighted by a learned radial representation. This sum is followed by an additional self-connection, then a residual self-connection. The output of the convolution is then passed through an equivariant non-linearity $\text{Gate}(\cdot)$ operation as described in [34]. We use SiLU and tanh activation functions for even and odd parity scalars respectively, as is done in [17].

Probe representations are updated similarly as the atoms for each layer, except their representations depend solely on the representations of neighboring atoms, with no probe-probe interaction. Each probe representation is updated with $P_k^{n+1} = \text{Gate}(\text{Conv}_{\text{probe}}^n(\vec{g}_k, P_k^n))$, where $\text{Conv}_{\text{probe}}$ is defined as:

$$\text{Conv}_{\text{probe}}^n(\vec{g}_k, P_k^n) = W_1^n \left(\sum_{i \in N(k)} W_2^n A_i^n \otimes R(r_{ik}) Y(\hat{r}_{ik}) \right) + W_3^n P_k^n . \quad (6)$$

Note that weights W are not shared with those for $\text{Conv}_{\text{atom}}^n(\cdot)$. Since atom representations are computed independently of probe positions, they can be computed once per atomic configuration, even if multiple batches are required to obtain predictions for all probe points. Finally, predicted charge density $\hat{\rho}(\vec{g}_k)$ is computed as a linear combination of the scalar elements of the final representation $P_k^{n=N_{\text{layers}}}$.

4.2 Training details

4.2.1 Optimization

Table A.1 outlines the experimental setup for training ChargE3Net on each of the datasets. All models For each gradient step, a random batch of materials is selected, from which a random subset of the charge density probe points are used. We use the Adam optimizer [35], and decay the learning rate by $0.96^{s/\beta}$ at step s . We find that optimizing for L1 error improves performance and training stability over mean squared error (see Table A.2).

4.2.2 Graph construction

We propose an algorithm to achieve more efficient atom-probe graph construction, enabling faster training and inference times. Prior work constructs graphs by adding probe points directly to the atomic structure, computing edges with atomic simulation software such as `ase` or `asap` [36], then removing edges between probes. While this is performant for small systems with few probes, we find it does not scale well due to the redundant computation of probe-probe edges, which grow quadratically with respect to the number of probe points. To address this, our algorithm leverages two k -d trees [37]; one to partition atoms, and one to partition probe points. This enables an efficient radius search for atom-probe edges exclusively. We implement this through modification of the k -d tree implementation `scipy` [38] to handle periodic boundary conditions. Constructing graphs with 1000 probe points, we observe an average graph construction time (\pm standard error) of 0.00758 ± 0.00087 , 0.0103 ± 0.0005 , and 0.00462 ± 0.00056 seconds for MP, QM9, and NMC respectively. This is at least an order of magnitude faster than methods from [11], with which we measured graph construction times of 12.6 ± 0.9 , 0.114 ± 0.006 , and 0.141 ± 0.010 seconds.

4.3 Datasets

The QM9 and NMC datasets, along with train, validation and test splits, are provided by Jørgensen and Bhowmik [11]. The QM9 dataset[23] contains VASP calculations of the 133,845 small organic molecules introduced by Ramakrishnan et al. [22], with training, validation, and test splits of size 123835, 50, and 10,000 respectively. The NMC dataset[24] consists of VASP calculations of 2000 randomly sampled nickel manganese cobalt oxides containing varying levels of lithium content, with training, validation, and test splits of size 1450, 50, and 500 respectively. For the MP data, we collected 122,689 structures and associated charge densities from api.materialsproject.org. Structures in the dataset that shared composition and space group were identified as duplicates and only the highest `material_id` structure was included, leaving 108,683 materials. The data was split into training, validation, and test splits with sizes 106,171, 512, and 2000 respectively. Later, analyzing the test set materials for thermodynamic stability and structural abnormalities (Fig. A.5), 26 materials were found to have unrealistic volume per atom, in excess of $100 \text{ \AA}^3/\text{atom}$ and mostly from space group *Immm*. These materials were removed from the test set and excluded from results.

4.4 Density Functional Theory calculations

All density functional theory (DFT) calculations were done with VASP version 5.4.4 [39–42] using projector-augmented wave (PAW) pseudopotentials [43]. For all calculations done on the test set of Materials Project data, we use the input files provided by the Materials Project to ensure these are computed in a manner consistent with how the charge density grids are originally generated. For the experiments with perturbed structures, including those where electronic and thermal properties were computed, we use all the same settings as the Materials Project but with different k-grids, all generated with the Monkhorst-Pack scheme unless otherwise specified. We use a 520 eV energy cutoff and converge each calculation until the change in energy between SCF steps is less than 10^{-5} eV . For the Si(111)-(2x1) calculation, we use a k-grid of 4x8x1, while all zeolite calculations were done at the gamma-point only. Electronic bandstructures were plotted using pymatgen [44]. We use the same Hubbard U values as the Materials Project, which were obtained from Wang et al. [45] and Jain et al. [46].

Thermal properties were computed using phonopy [47, 48] for the heat capacity. Zeolite and bulk Si structures were relaxed until the maximum norm of the Hellmann-Feynman forces fell below 0.001 eV/\AA prior to computing thermal properties. Structures were perturbed by 0.03\AA to find the Hessian of the potential energy surface via finite differences, and the heat capacity at constant volume can then be found via the harmonic approximation with the equation

$$C_v(T) = R \sum_k \exp(\theta_k/T) \left(\frac{\theta_k/T}{\exp(\theta_k/T) - 1} \right) \quad (7)$$

where $\theta_k = h\nu_k/k_B$, h is Planck's constant, ν_k is the vibrational frequency of vibrational mode k , k_B is Boltzmann's constant, R is the gas constant, and T is the temperature in Kelvin.

5 Data availability

Materials Project data was collected 7 May 2023. Associated task identifiers will be included in our provided repository, along with the necessary download script, and our train, validation, and test splits. VASP computations on the QM9 and NMC datasets were downloaded from Jørgensen and Bhowmik [23] and Jørgensen and Bhowmik [24] respectively.

6 Code availability

Our model implementation, along with pretrained model weights is available at <https://github.com/AIforGreatGood/charge3net>.

Declarations

Acknowledgements

We thank Tess Smidt and Mark Polking for helpful discussions.

DISTRIBUTION STATEMENT A. Approved for public release. Distribution is unlimited. This material is based upon work supported by the Under Secretary of Defense for Research and Engineering under Air Force Contract No. FA8702-15-D-0001. Any opinions, findings, conclusions or recommendations expressed in this material are those of the author(s) and do not necessarily reflect the views of the Under Secretary of Defense for Research and Engineering. © 2023 Massachusetts Institute of Technology. Delivered to the U.S. Government with Unlimited Rights, as defined in DFARS Part 252.227-7013 or 7014 (Feb 2014). Notwithstanding any copyright notice, U.S. Government rights in this work are defined by DFARS 252.227-7013 or DFARS 252.227-7014 as detailed above. Use of this work other than as specifically authorized by the U.S. Government may violate any copyrights that exist in this work.

Author Contributions

T.K. designed, implemented, and trained the ChargE3Net models. K.Q. collected and prepared the MP, QM9, and NMC datasets, and contributed to the software implementation and training of baseline models. K.Q. devised

the angular variation metric and performed analysis on the effects of rotation order together with T.K. E.T. performed experimentation and analysis for initialization of DFT calculations and non-self-consistent calculation of material properties. K.T. provided guidance on DFT calculations. L.L. conceived the project, supervised the research and advised experimentation and data analysis. All authors contributed to the writing and editing of the manuscript.

Competing interests

All authors T.K., K.Q., E.T., K.T. and L.L. declare no financial and non-financial competing interests.

References

- [1] P. Hohenberg and W. Kohn. Inhomogeneous electron gas. *Physical Review*, 136(3B):B864–B871, November 1964. doi: 10.1103/PhysRev.136.B864.
- [2] W. Kohn and L. J. Sham. Self-consistent equations including exchange and correlation effects. *Physical Review*, 140(4A):A1133–A1138, November 1965. doi: 10.1103/PhysRev.140.A1133.
- [3] Andrea Grisafi, Alberto Fabrizio, Benjamin Meyer, David M Wilkins, Clemence Corminboeuf, and Michele Ceriotti. Transferable machine-learning model of the electron density. *ACS central science*, 5(1):57–64, 2018.
- [4] Alberto Fabrizio, Andrea Grisafi, Benjamin Meyer, Michele Ceriotti, and Clemence Corminboeuf. Electron density learning of non-covalent systems. *Chemical science*, 10(41):9424–9432, 2019.
- [5] Zhuoran Qiao, Anders S Christensen, Matthew Welborn, Frederick R Manby, Anima Anandkumar, and Thomas F Miller III. Informing geometric deep learning with electronic interactions to accelerate quantum chemistry. *Proceedings of the National Academy of Sciences*, 119(31): e2205221119, 2022.
- [6] Stefan Grimme, Christoph Bannwarth, and Philip Shushkov. A robust and accurate tight-binding quantum chemical method for structures, vibrational frequencies, and noncovalent interactions of large molecular systems parametrized for all spd-block elements (Z= 1–86). *Journal of chemical theory and computation*, 13(5):1989–2009, 2017.
- [7] Joshua A Rackers, Lucas Tecot, Mario Geiger, and Tess E Smidt. A recipe for cracking the quantum scaling limit with machine learned electron densities. *Machine Learning: Science and Technology*, 4(1):015027, 2023.
- [8] Loredana Edith Daga, Bartolomeo Civalleri, and Lorenzo Maschio. Gaussian Basis Sets for Crystalline Solids: All-Purpose Basis Set Libraries vs

System-Specific Optimizations. *Journal of Chemical Theory and Computation*, 16(4):2192–2201, April 2020. ISSN 1549-9618. doi: 10.1021/acs.jctc.9b01004.

- [9] Sheng Gong, Tian Xie, Taishan Zhu, Shuo Wang, Eric R Fadel, Yawei Li, and Jeffrey C Grossman. Predicting charge density distribution of materials using a local-environment-based graph convolutional network. *Physical Review B*, 100(18):184103, 2019.
- [10] Peter Bjørn Jørgensen and Arghya Bhowmik. DeepDFT: Neural message passing network for accurate charge density prediction. *arXiv preprint arXiv:2011.03346*, 2020.
- [11] Peter Bjørn Jørgensen and Arghya Bhowmik. Equivariant graph neural networks for fast electron density estimation of molecules, liquids, and solids. *npj Computational Materials*, 8(1):183, 2022.
- [12] Ethan M. Sunshine, Muhammed Shuaibi, Zachary W. Ulissi, and John R. Kitchin. Chemical Properties from Graph Neural Network-Predicted Electron Densities. *The Journal of Physical Chemistry C*, November 2023. ISSN 1932-7447. doi: 10.1021/acs.jpcc.3c06157.
- [13] Tian Xie and Jeffrey C Grossman. Crystal graph convolutional neural networks for an accurate and interpretable prediction of material properties. *Physical review letters*, 120(14):145301, 2018.
- [14] Kristof Schütt, Pieter-Jan Kindermans, Huziel Enoc Sauceda Felix, Stefan Chmiela, Alexandre Tkatchenko, and Klaus-Robert Müller. Schnet: A continuous-filter convolutional neural network for modeling quantum interactions. *Advances in neural information processing systems*, 30, 2017.
- [15] Kristof Schütt, Oliver Unke, and Michael Gastegger. Equivariant message passing for the prediction of tensorial properties and molecular spectra. In *International Conference on Machine Learning*, pages 9377–9388. PMLR, 2021.
- [16] Jimmy-Xuan Shen, Jason M Munro, Matthew K Horton, Patrick Huck, Shyam Dwaraknath, and Kristin A Persson. A representation-independent electronic charge density database for crystalline materials. *Scientific Data*, 9(1):661, 2022.
- [17] Simon Batzner, Albert Musaelian, Lixin Sun, Mario Geiger, Jonathan P Mailoa, Mordechai Kornbluth, Nicola Molinari, Tess E Smidt, and Boris Kozinsky. E (3)-Equivariant graph neural networks for data-efficient and accurate interatomic potentials. *Nature communications*, 13(1):2453, 2022.
- [18] Sergey N Pozdnyakov and Michele Ceriotti. Incompleteness of graph neural networks for points clouds in three dimensions. *Machine Learning: Science and Technology*, 3(4):045020, 2022.

- [19] Nathaniel Thomas, Tess Smidt, Steven Kearnes, Lusann Yang, Li Li, Kai Kohlhoff, and Patrick Riley. Tensor field networks: Rotation-and translation-equivariant neural networks for 3d point clouds. *arXiv preprint arXiv:1802.08219*, 2018.
- [20] Mario Geiger and Tess Smidt. E3nn: Euclidean neural networks, 2022.
- [21] Lars Ruddigkeit, Ruud Van Deursen, Lorenz C Blum, and Jean-Louis Raymond. Enumeration of 166 billion organic small molecules in the chemical universe database GDB-17. *Journal of chemical information and modeling*, 52(11):2864–2875, 2012.
- [22] Raghunathan Ramakrishnan, Pavlo O Dral, Matthias Rupp, and O Anatole Von Lilienfeld. Quantum chemistry structures and properties of 134 kilo molecules. *Scientific data*, 1(1):1–7, 2014.
- [23] Peter Bjørn Jørgensen and Arghya Bhowmik. QM9 charge densities and energies calculated with VASP. August 2022. doi: 10.11583/DTU.16794500. v1.
- [24] Peter Bjørn Jørgensen and Arghya Bhowmik. NMC li-ion battery cathode energies and charge densities. August 2022. doi: 10.11583/DTU.16837721. v1.
- [25] Anubhav Jain, Shyue Ping Ong, Geoffroy Hautier, Wei Chen, William Davidson Richards, Stephen Dacek, Shreyas Cholia, Dan Gunter, David Skinner, Gerbrand Ceder, et al. Commentary: The Materials Project: A materials genome approach to accelerating materials innovation. *APL materials*, 1(1), 2013.
- [26] Saro Passaro and C Lawrence Zitnick. Reducing SO (3) convolutions to SO (2) for efficient equivariant GNNs. *arXiv preprint arXiv:2302.03655*, 2023.
- [27] David S. Sholl and Janice A. Steckel. *Density Functional Theory*. John Wiley & Sons, Ltd, 1 edition, 2009. ISBN 978-0-470-37317-0. doi: 10.1002/9780470447710.
- [28] Susi Lehtola. Assessment of Initial Guesses for Self-Consistent Field Calculations. Superposition of Atomic Potentials: Simple yet Efficient. *Journal of Chemical Theory and Computation*, 15(3):1593–1604, March 2019. ISSN 1549-9618. doi: 10.1021/acs.jctc.8b01089.
- [29] John A. Pople. Nobel Lecture: Quantum chemical models. *Reviews of Modern Physics*, 71(5):1267–1274, October 1999. doi: 10.1103/RevModPhys.71.1267.
- [30] Dahvyd Wing, Guy Ohad, Jonah B. Haber, Marina R. Filip, Stephen E. Gant, Jeffrey B. Neaton, and Leeor Kronik. Band gaps of crystalline solids from Wannier-localization-Based optimal tuning of a screened range-separated hybrid functional. *Proceedings of the National Academy of Sciences*, 118(34):e2104556118, August 2021. doi: 10.1073/pnas.2104556118.

- [31] Matthew Kristofer Horton, Joseph Harold Montoya, Miao Liu, and Kristin Aslaug Persson. High-throughput prediction of the ground-state collinear magnetic order of inorganic materials using Density Functional Theory. *npj Computational Materials*, 5(1):1–11, June 2019. ISSN 2057-3960. doi: 10.1038/s41524-019-0199-7.
- [32] Kyuhyun Lee, Yong Youn, and Seungwu Han. Identification of ground-state spin ordering in antiferromagnetic transition metal oxides using the Ising model and a genetic algorithm. *Science and Technology of Advanced Materials*, 18(1):246–252, December 2017. ISSN 1468-6996. doi: 10.1080/14686996.2017.1300046.
- [33] Dan Hendrycks and Kevin Gimpel. Gaussian error linear units (gelus). *arXiv preprint arXiv:1606.08415*, 2016.
- [34] Maurice Weiler, Mario Geiger, Max Welling, Wouter Boomsma, and Taco S Cohen. 3d steerable cnns: Learning rotationally equivariant features in volumetric data. *Advances in Neural Information Processing Systems*, 31, 2018.
- [35] Diederik P Kingma and Jimmy Ba. Adam: A method for stochastic optimization. *arXiv preprint arXiv:1412.6980*, 2014.
- [36] Ask Hjorth Larsen, Jens Jørgen Mortensen, Jakob Blomqvist, Ivano E Castelli, Rune Christensen, Marcin Dulak, Jesper Friis, Michael N Groves, Bjørk Hammer, Cory Hargus, et al. The atomic simulation Environment—a Python library for working with atoms. *Journal of Physics: Condensed Matter*, 29(27):273002, 2017.
- [37] Jon Louis Bentley. Multidimensional binary search trees used for associative searching. *Communications of the ACM*, 18(9):509–517, 1975.
- [38] Pauli Virtanen, Ralf Gommers, Travis E. Oliphant, Matt Haberland, Tyler Reddy, David Cournapeau, Evgeni Burovski, Pearu Peterson, Warren Weckesser, Jonathan Bright, Stéfan J. van der Walt, Matthew Brett, Joshua Wilson, K. Jarrod Millman, Nikolay Mayorov, Andrew R. J. Nelson, Eric Jones, Robert Kern, Eric Larson, C J Carey, İlhan Polat, Yu Feng, Eric W. Moore, Jake VanderPlas, Denis Laxalde, Josef Perktold, Robert Cimrman, Ian Henriksen, E. A. Quintero, Charles R. Harris, Anne M. Archibald, Antônio H. Ribeiro, Fabian Pedregosa, Paul van Mulbregt, and SciPy 1.0 Contributors. SciPy 1.0: Fundamental algorithms for scientific computing in python. *Nature Methods*, 17:261–272, 2020. doi: 10.1038/s41592-019-0686-2.
- [39] Jürgen Hafner. Ab-initio simulations of materials using VASP: Density-functional theory and beyond. *Journal of computational chemistry*, 29(13): 2044–2078, 2008.

- [40] G. Kresse and J. Hafner. Ab initio molecular dynamics for liquid metals. *Physical Review B*, 47(1):558–561, January 1993. doi: 10.1103/PhysRevB.47.558.
- [41] G. Kresse and J. Furthmüller. Efficiency of ab-initio total energy calculations for metals and semiconductors using a plane-wave basis set. *Computational Materials Science*, 6(1):15–50, July 1996. ISSN 0927-0256. doi: 10.1016/0927-0256(96)00008-0.
- [42] G. Kresse and J. Furthmüller. Efficient iterative schemes for ab initio total-energy calculations using a plane-wave basis set. *Physical Review B*, 54(16): 11169–11186, October 1996. doi: 10.1103/PhysRevB.54.11169.
- [43] G. Kresse and D. Joubert. From ultrasoft pseudopotentials to the projector augmented-wave method. *Physical Review B*, 59(3):1758–1775, January 1999. doi: 10.1103/PhysRevB.59.1758.
- [44] Shyue Ping Ong, William Davidson Richards, Anubhav Jain, Geoffroy Hautier, Michael Kocher, Shreyas Cholia, Dan Gunter, Vincent L. Chevrier, Kristin A. Persson, and Gerbrand Ceder. Python Materials Genomics (pymatgen): A robust, open-source python library for materials analysis. *Computational Materials Science*, 68:314–319, February 2013. ISSN 0927-0256. doi: 10.1016/j.commatsci.2012.10.028.
- [45] Lei Wang, Thomas Maxisch, and Gerbrand Ceder. Oxidation energies of transition metal oxides within the $\mathrm{GGA}+\mathrm{U}$ framework. *Physical Review B*, 73(19):195107, May 2006. doi: 10.1103/PhysRevB.73.195107.
- [46] Anubhav Jain, Geoffroy Hautier, Shyue Ping Ong, Charles J. Moore, Christopher C. Fischer, Kristin A. Persson, and Gerbrand Ceder. Formation enthalpies by mixing GGA and GGA $+\mathrm{U}$ calculations. *Physical Review B*, 84(4):045115, July 2011. doi: 10.1103/PhysRevB.84.045115.
- [47] Atsushi Togo, Laurent Chaput, Terumasa Tadano, and Isao Tanaka. Implementation strategies in phonopy and phono3py. *Journal of Physics: Condensed Matter*, 35(35):353001, 2023. doi: 10.1088/1361-648X/acd831.
- [48] Atsushi Togo. First-principles phonon calculations with phonopy and phono3py. *Journal of The Physical Society of Japan*, 92(1):012001, 2023. doi: 10.7566/JPSJ.92.012001.
- [49] J. B. Parise, D. R. Corbin, L. Abrams, and D. E. Cox. Structure of dealuminated Linde Y-zeolite; $\mathrm{Si}_{139.7}\mathrm{Al}_{52.3}\mathrm{O}_{384}$ and $\mathrm{Si}_{173.1}\mathrm{Al}_{18.9}\mathrm{O}_{384}$: Presence of non-framework Al species. *Acta Crystallographica Section C: Crystal Structure Communications*, 40(9):1493–1497, September 1984. ISSN 0108-2701. doi: 10.1107/S0108270184008490.

- [50] George N. Nikolaidis, Eustathios S. Kikkinides, and Michael C. Georgiadis. A model-based approach for the evaluation of new zeolite 13X-based adsorbents for the efficient post-combustion CO₂ capture using P/VSA processes. *Chemical Engineering Research and Design*, 131:362–374, March 2018. ISSN 0263-8762. doi: 10.1016/j.cherd.2017.06.016.
- [51] John Young, Fergus Mcilwaine, Berend Smit, Susana Garcia, and Mijndert van der Spek. Process-informed adsorbent design guidelines for direct air capture. *Chemical Engineering Journal*, 456:141035, January 2023. ISSN 1385-8947. doi: 10.1016/j.cej.2022.141035.
- [52] Seyed Mohamad Moosavi, Balázs Álmos Novotny, Daniele Ongari, Elias Moubarak, Mehrdad Asgari, Özge Kadioglu, Charitha Charalambous, Andres Ortega-Guerrero, Amir H. Farmahini, Lev Sarkisov, Susana Garcia, Frank Noé, and Berend Smit. A data-science approach to predict the heat capacity of nanoporous materials. *Nature Materials*, 21(12):1419–1425, December 2022. ISSN 1476-4660. doi: 10.1038/s41563-022-01374-3.
- [53] Manish Jain, James R. Chelikowsky, and Steven G. Louie. Reliability of Hybrid Functionals in Predicting Band Gaps. *Physical Review Letters*, 107 (21):216806, November 2011. doi: 10.1103/PhysRevLett.107.216806.

A Supplementary Information

A.1 Heat capacity and thermal conductivity of faujasite

Computing thermal properties of materials require knowing the phonon modes of the material. A typical approach to finding phonon modes and their corresponding vibrational frequencies is to first compute the Hessian of the total energy with respect to the atomic positions, yielding a second-order (harmonic) approximation to the potential energy surface. The Hessian can be found via finite differences, and the number of displacements required scales with the size of the system under study. These computationally intensive calculations may be made cheaper with accurate charge density estimates from ChargE3Net, and we show that the charge density predictions are robust to small perturbations of atomic positions (see Figure A.6). Below, we further show that even non-self-consistent calculations of thermal properties with these estimates yield near-perfect agreement with self-consistent calculations of the same.

We evaluate two variants of faujasite zeolite, one that is purely composed of Si and O (USY) [49], and another where a portion of the Si sites are exchanged with Al charge-balanced by Na ions (NaX). The structures of these are shown in A.14. Understanding the thermal properties of porous materials such as these via data-driven predictive models could aid high-throughput screening of gas adsorbents for industrially relevant separation processes such as carbon capture [50–52]. We note that while the elemental compositions of USY and NaX (Si-O and Na-Al-Si-O, respectively) exist in the Materials Project dataset, porous zeolites are not found in the dataset. Despite this, we show that the constant-volume heat capacity (C_v) obtained via the harmonic approximation from non-self-consistent calculations on ChargE3Net’s predicted charge densities closely resemble the C_v obtained by self-consistent DFT (see Figure A.15). Charge density predictions of USY and NaX had an average ϵ_{mae} of 0.16% and 0.58%, respectively. This demonstrates ChargE3Net’s ability to obtain accurate macroscopic properties of unseen structures by predicting local perturbations to the charge density

A.2 Electronic bandstructure of Si surface

DFT calculations on material surfaces are highly important for understanding catalytic reactions, material interfaces, and corrosion [27]. Because surfaces are not part of the training set, obtaining accurate charge densities from ChargE3Net shows one example of the model’s ability to generalize to unseen atomic environments.

Pandey shows through tight-binding calculations that the Si(111)-(2x1) surface, the structure of which is plotted in A.16, is characterized by pairs of Si sites that undergo significant bond rearrangement to form zig-zag patterns of raised Si atoms. These pairs form chains of π -bonds across the surface. While multiple polymorphs of Si, both experimentally-observed and hypothesized, are catalogued in the Materials Project and part of the training set, ChargE3Net

was not trained on any Si surface charge densities. We obtain the structure of the surface model from [53], and in Figure A.17, we show that a non-self-consistent (NSC) calculation using the charge density output by ChargeE3Net reproduces almost exactly the electronic bandstructure of a self-consistent (SC) DFT calculation. Interestingly, even the bands corresponding to the surface Si sites at the valence band maximum and conduction band minimum are accurately reproduced, indicating the model is capable of extrapolating the charge density grid in a physically meaningful way despite new atomic environments such as 3-coordinate surface Si sites. The ϵ_{mae} of the predicted charge density is approximately 0.83%, and the distribution of charge density prediction error is shown in A.16.

Table A.1: Training setup

Dataset	Learning Rate	Decay β	L	Batch Size	Training Steps
NMC	0.01	10^4	4	8 * 200 points	$7.5 * 10^5$
QM9	0.01	10^4	4	8 * 200 points	10^6
MP	0.005	$3 * 10^3$	4	16 * 200 points	10^6

Table A.2: Loss function ablation, reported in average ϵ_{mae} (%), \pm one standard error.

Loss Function	MP	QM9	NMC
MSE	0.722 ± 0.011	0.268 ± 0.001	0.076 ± 0.001
L1	0.523 ± 0.010	0.196 ± 0.001	0.060 ± 0.001

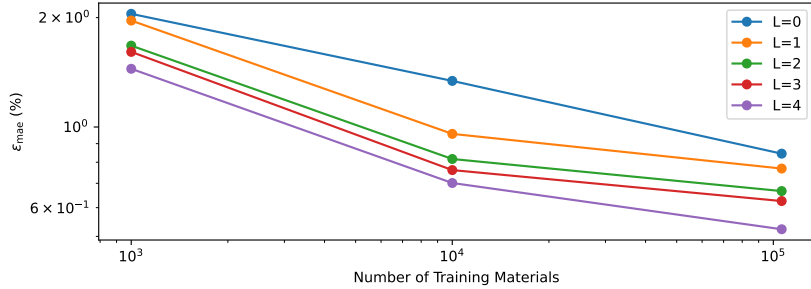


Figure A.1: Log-log plot of training set size vs performance, measured in average ϵ_{mae} (%) on the Materials Project test set. We show models train with maximum rotation order $L \in \{0, 1, 2, 3, 4\}$.

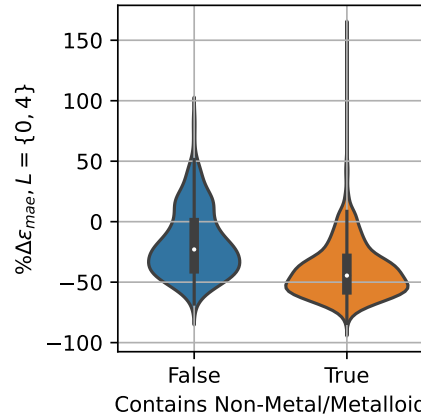


Figure A.2: Violin plot of the percent change in ϵ_{mae} (%) from the $L = 0$ to $L = 4$ model for test set materials. 1648 materials contain either a non-metal or a metalloid (orange), while 346 materials are composed of only metals (blue).

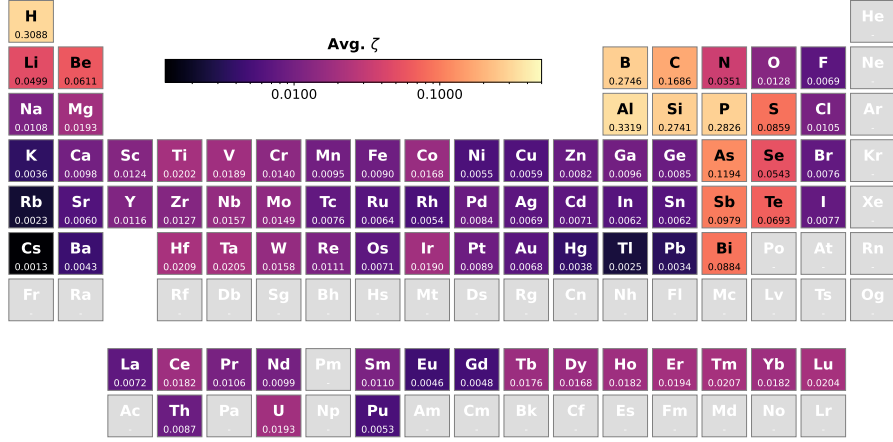


Figure A.3: Average ζ , computed on DFT-computed charge density at probe points $G_{local,i}$ for each element. Only elements contained in at least 10 test set materials shown.

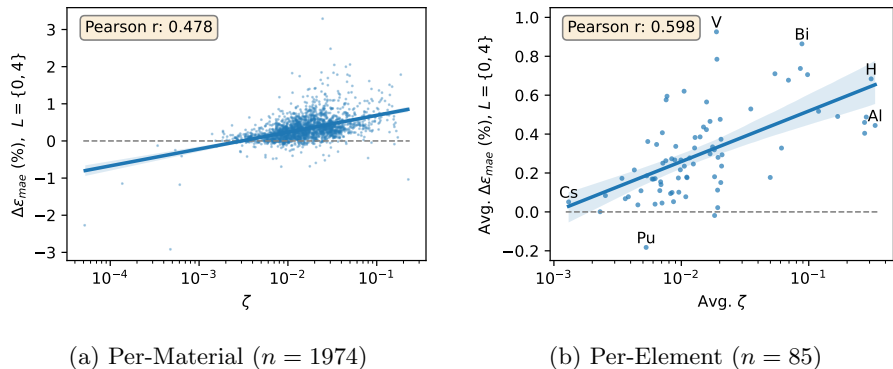


Figure A.4: $\Delta\epsilon_{mae}$ (improvement from $L = 0$ to $L = 4$) vs. ζ , on a per-material (left) and per-element (right) basis. For per-element results, the ϵ_{mae} and ζ values are computed over the set of grid points G_{local} , and averaged across all materials containing that element. Only those elements in at least 10 test materials are shown.

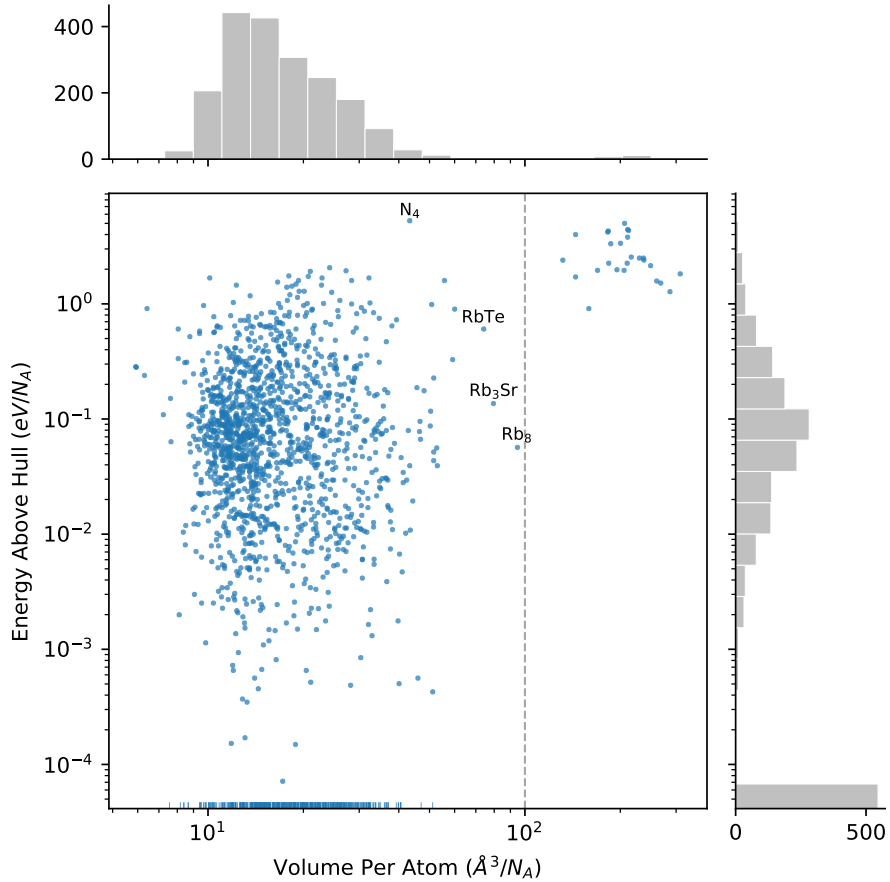


Figure A.5: Scatterplot of test set Energy Above Hull vs Volume Per Atom ($n = 2000$). 26 materials in excess of $100 \text{\AA}^3/N_A$ (dashed line) were removed from the test set for other calculations. Of those removed, 25 are in space group *I*₄*m*₃*m* and one is in *C*₂*m*₂*m*. Thermodynamically stable materials ($0.0 \text{ eV}/N_A$) are plotted along the x axis.

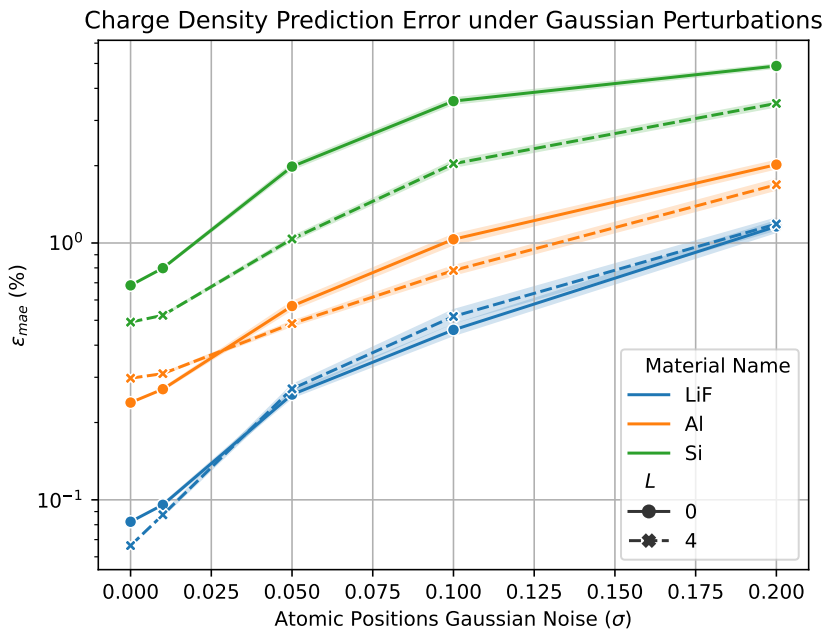


Figure A.6: ϵ_{mae} as a function of perturbations of atomic positions for LiF (mp-1138, blue), Al (mp-134, orange), and Si (mp-149, green). Solid lines represent the $L = 0$ variant of ChargE3Net, while dashed lines represent the $L = 4$ variant of ChargE3Net. We compute self-consistent DFT calculations with atomic positions $r' = r + \delta$, where r is the original position of the atoms from the Materials Project and $\delta \sim \mathcal{N}(0, \sigma)$. These are used as the ground truth charge densities which we use to compare with ChargE3Net's predictions.

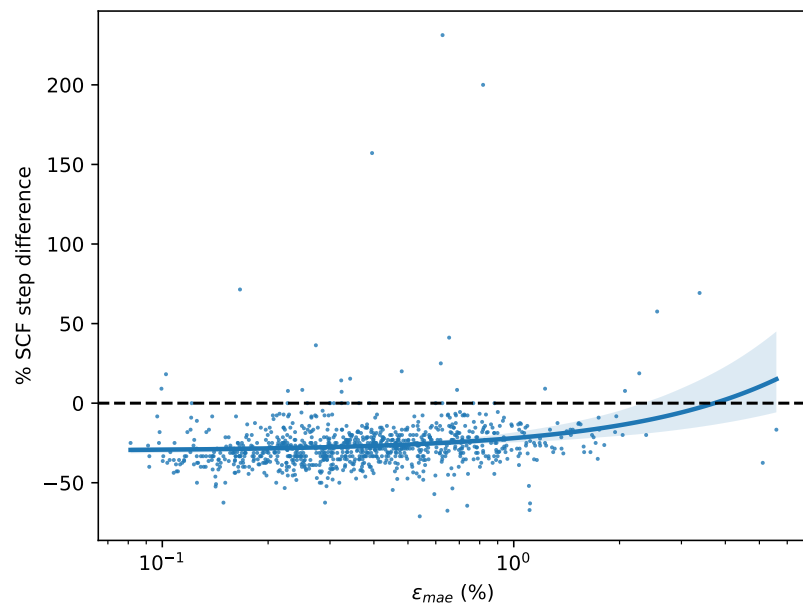


Figure A.7: ϵ_{mae} plotted against the percent improvement in the number of SCF steps needed to reach self-consistency. Pearson $r \approx 0.19$ for the correlation between ϵ_{mae} and % SCF step difference.

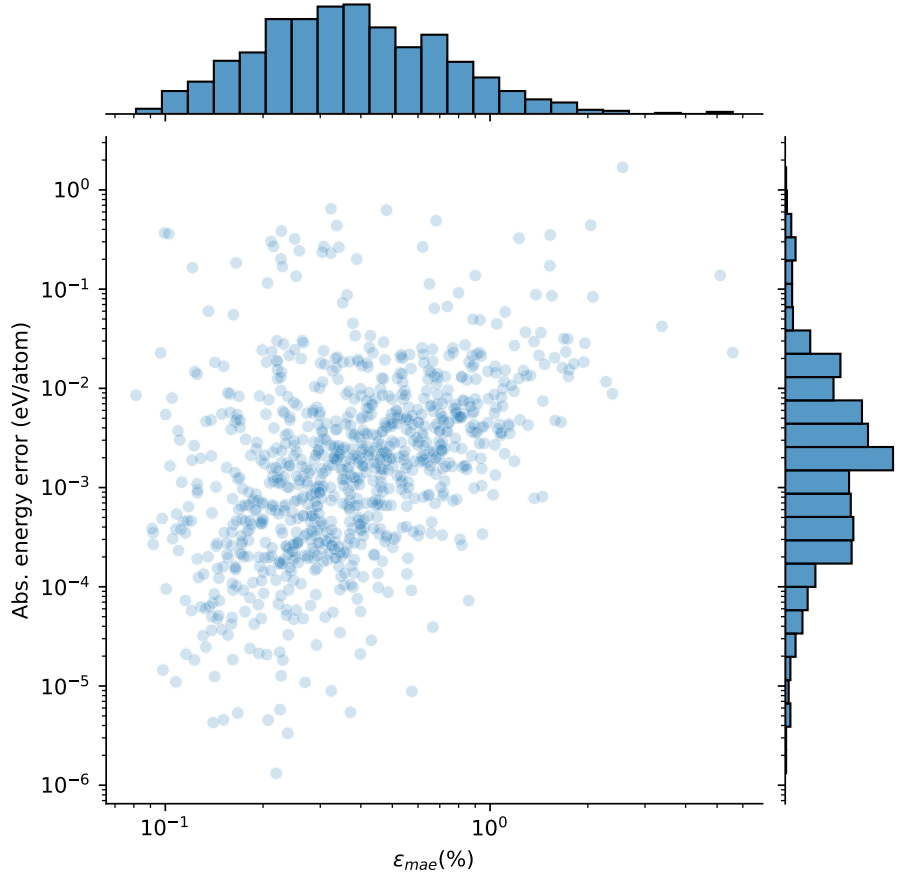


Figure A.8: Per-atom energy absolute error between non-self-consistent calculations on ChargE3Net’s charge density predictions and self-consistent calculations plotted against ϵ_{mae} of the test set. The distributions of the per-atom energy error and ϵ_{mae} are on the right and top of the plot, respectively. Pearson $r \approx 0.44$ for $\log \epsilon_{mae}$ vs. log energy error.

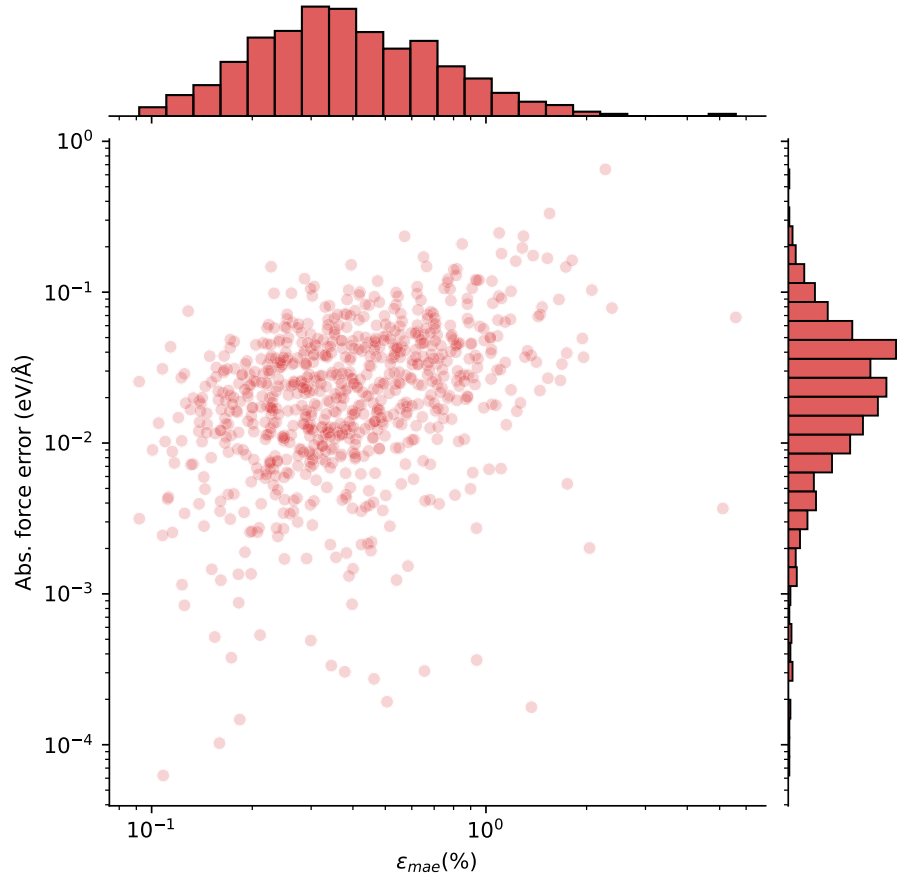
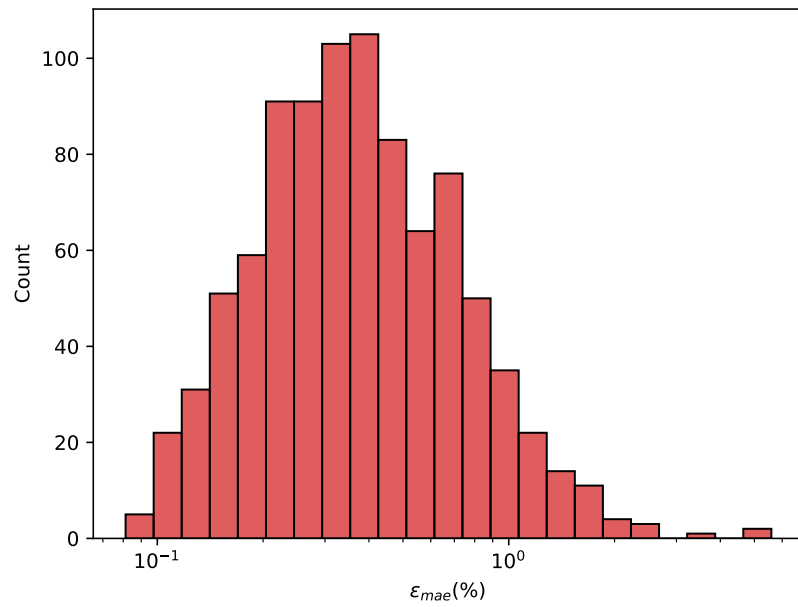


Figure A.9: Average force absolute error between non-self-consistent calculations on ChargeE3Net’s charge density predictions and self-consistent calculations plotted against ϵ_{mae} of the test set. The distributions of the force error and ϵ_{mae} are on the right and top of the plot, respectively. 15% of structures achieved perfect agreement with the ground-truth self-consistent calculation, which are not shown in this plot. See A.10 for the distribution of ϵ_{mae} of these structures. Pearson $r \approx 0.35$ for $\log \epsilon_{mae}$ vs. \log force error.



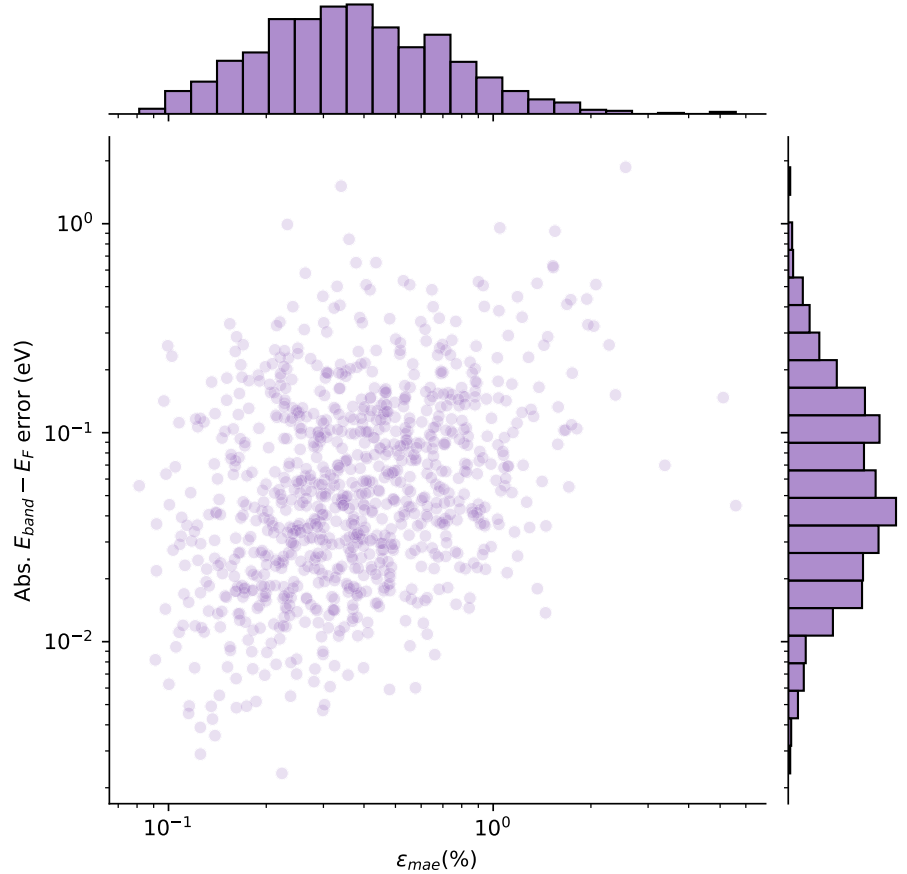


Figure A.11: Band energy (eigenvalue) absolute error between non-self-consistent calculations on ChargE3Net's charge density predictions and self-consistent calculations plotted against ϵ_{mae} of the test set. The distributions of the band energy error and ϵ_{mae} are on the right and top of the plot, respectively. Pearson $r \approx 0.35$ for $\log \epsilon_{mae}$ vs. \log band energy error.

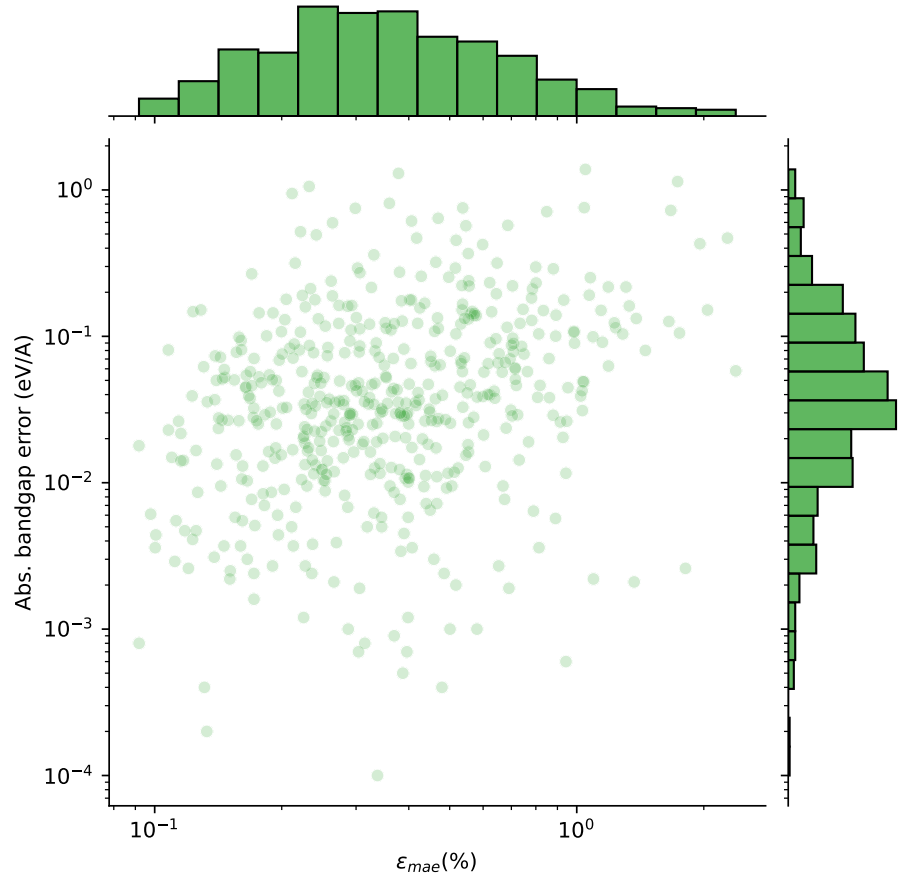


Figure A.12: Band gap absolute error between non-self-consistent calculations on ChargeE3Net’s charge density predictions and self-consistent calculations plotted against ϵ_{mae} of the test set. The distributions of the band gap error and ϵ_{mae} are on the right and top of the plot, respectively. About 43% of structures achieve perfect band gap agreement with self-consistent calculations, which are not shown in this plot, and the distribution of their ϵ_{mae} is plotted in A.13. Pearson $r \approx 0.29$ for $\log \epsilon_{mae}$ vs. \log band gap error.

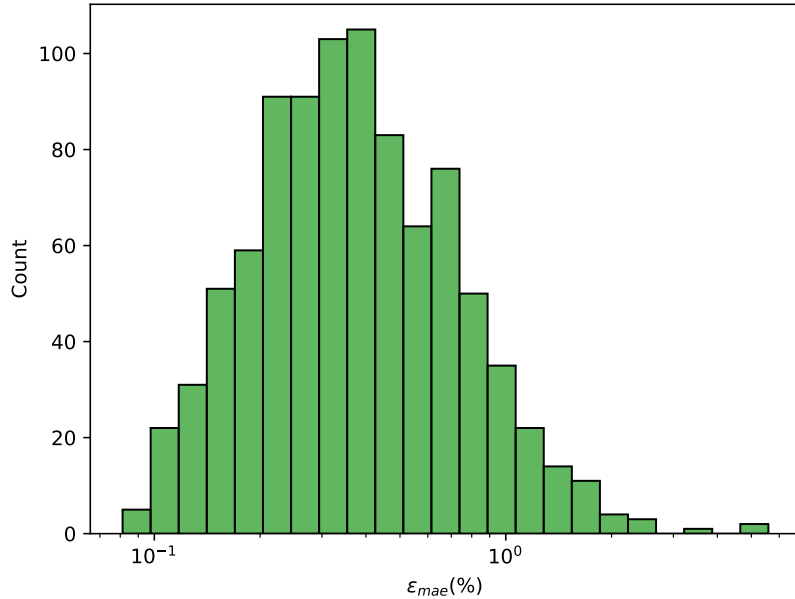


Figure A.13: Distribution of ϵ_{mae} where each structure has a perfect band gap agreement between a non-self-consistent calculation initialized with ChargeE3Net's prediction and a self-consistent calculation.

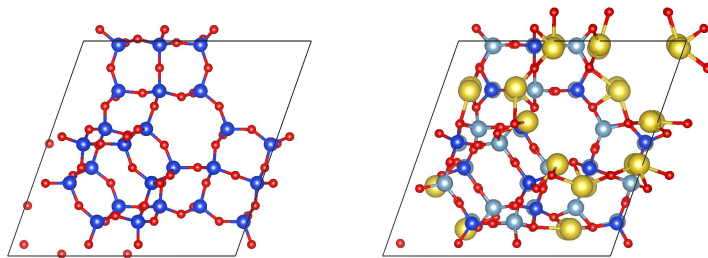


Figure A.14: Structural models of (right) USY and (left) NaX zeolites, two types of faujasite zeolites. Blue = Si, red = O, grey = Al, yellow = Na.

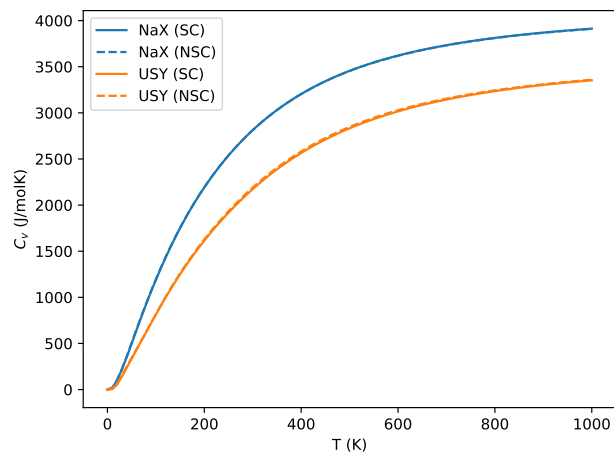


Figure A.15: Constant-volume heat capacity as a function of temperature as computed from self-consistent DFT calculations and non-self-consistent calculations on the predicted charge densities. Blue curves are for NaX and orange curves are for USY. Solid curves are computed via self-consistent DFT calculations of atomic displacements, while dashed curves are computed via non-self-consistent DFT calculations using ChargeE3Net's predicted charge densities of the same.

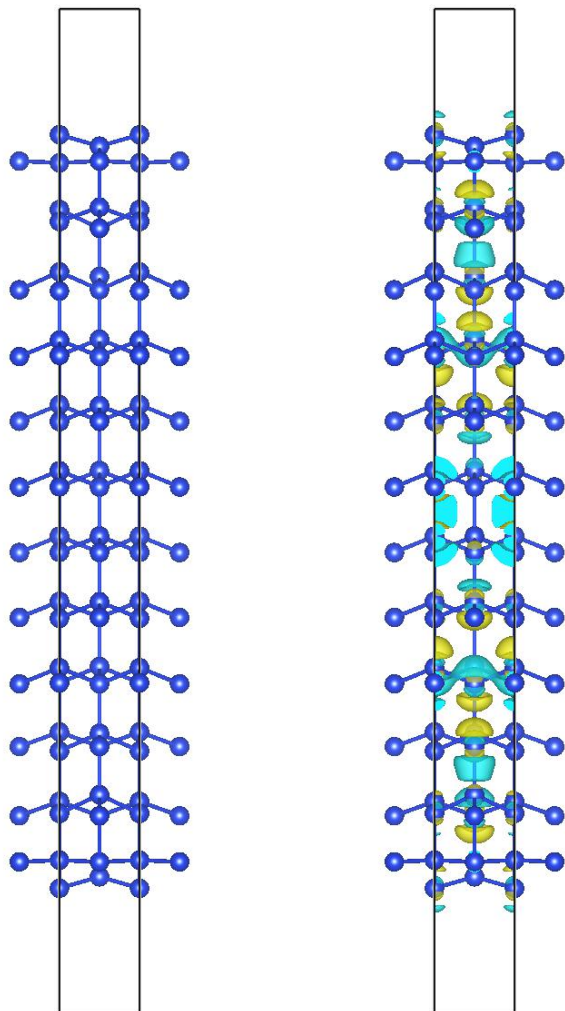


Figure A.16: (right) Structural model of a Si(111)-(2x1) surface, and (left) an isosurface of the charge density error overlayed on the structural model. Yellow denotes overestimation while teal denotes underestimation. The isosurface level used here is approximately 1.6×10^{-6} .

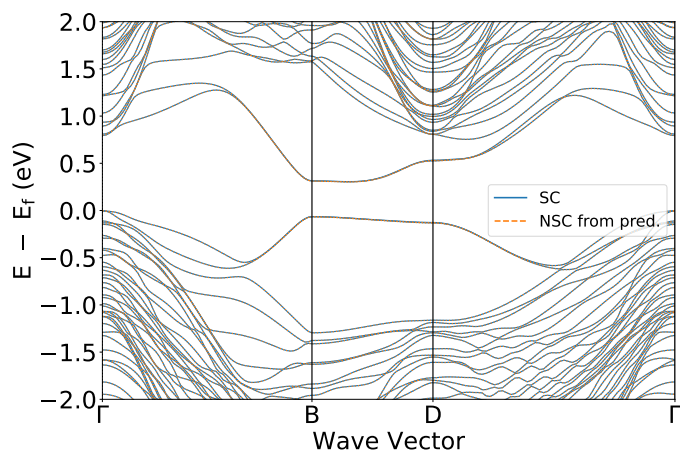


Figure A.17: Electronic bandstructure of Si(111)-(2x1) surface. Blue represents a self-consistent (SC) DFT calculation with the PBE exchange-correlation functional, and orange represents a non-self-consistent (NSC) calculation using the charge density predicted by ChargeE3Net with the same functional.